Nonlinear Dyn (2020) 102:1285–1296
https://doi.org/10.1007/s11071-020-06008-4

ORIGINAL PAPER

Bistable attachments for wideband nonlinear vibration attenuation in a metamaterial beam

Yiwei Xia · Massimo Ruzzene · Alper Erturk

Received: 5 August 2020 / Accepted: 7 October 2020 / Published online: 14 October 2020

Abstract This work investigates the amplitude-dependent dynamics of a locally resonant metamaterial beam with bistable attachments. The concept that was previously demonstrated for a discrete chain is extended to a continuous system, and the enhancement in vibration attenuation bandwidth is investigated through a cantilever beam under base excitation. The analysis approach combines the harmonic balance method and time-domain numerical integration to capture periodic and aperiodic responses for up-sweep and down-sweep harmonic excitation. The bistable attachments are shown to exhibit linear intrawell, nonlinear intrawell and nonlinear interwell oscillations for low, moderate, and high base acceleration levels. As a result, the metastructure leverages linear locally resonant bandgap under low excitation intensity, and nonlinear wideband attenuation due to chaotic vibrations of the bistable attachments under high excitation intensity. This is first demonstrated through frequency sweep numerical simulations for a broad range of excitation amplitudes. Experimental validations are then presented for a base-excited cantilever beam hosting seven magnetoelastic beam attachments. For moderate-to-high amplitude excitation levels, the interwell oscillations of the attachments produce an attenuation frequency range that is 350% wider than the corresponding linear locally resonant bandgap (observed for low-amplitude excitation levels), yielding the suppression of modes outside the bandgap with increased excitation intensity.

Keywords Metamaterials · Vibration · Bistability · Nonlinear

Electronic supplementary material The online version of this article (https://doi.org/10.1007/s11071-020-06008-4) contains supplementary material, which is available to authorized users.

Y. Xia (✉) · A. Erturk
George W. Woodruff School of Mechanical Engineering, Georgia Institute of Technology, Atlanta 30332, USA
e-mail: yxia63@gatech.edu
A. Erturk
e-mail: alper.erturk@me.gatech.edu

M. Ruzzene
Department of Mechanical Engineering, University of Colorado Boulder, Boulder 80309, USA
e-mail: Massimo.Ruzzene@colorado.edu

1 Introduction

Locally resonant (LR) metamaterials and resulting finite LR metastructures have been extensively studied over the past two decades since the seminal work by Liu et al. [1]. In LR metamaterials, the out-of-phase motion of the local resonators with respect to the base structure leads to the attenuation, typically occurring at the resonant frequency of the attachments. Therefore, LR bandgaps can happen at wavelengths much larger than the lattice size, yielding low-frequency vibration/noise attenuation and wave filtering [1–8]. However, most investigations have considered using linear local resonators. In such linear configurations, the resulting

attenuation bandwidth (LR bandgap size) is limited by the added mass [9], which is typically aimed to be minimized in most applications that require lightweight and compact designs due to space and weight limitations.

Compared to linear configurations, nonlinearities provide rich dynamics such as sub- and super-harmonic resonances and in some cases chaotic behavior. As leveraged in the vibration energy harvesting field, properly designed nonlinear oscillators offer various advantages, among which substantially enhanced frequency bandwidth is of primary interest. For instance, as summarized in [10], both monostable and bistable nonlinear oscillators have been investigated to enable wideband energy harvesters over the past decade. Especially, the bistable configurations provide a plethora of wideband dynamic behavior through periodic intrawell and interwell oscillations, and chaotic interwell vibrations depending on the input amplitudes [11–14]. These studies shed light on the design of individual bistable oscillators to target a specific frequency bandwidth, not only for harvesting energy but also for other applications.

In terms of nonlinear vibration attenuation, many efforts have focused on the concept of nonlinear energy sink (NES) [15–20], evolving from relatively simple systems of one linear oscillator with one NES attached to a continuous structure with one NES attached. In addition, some researchers utilized bistable oscillators; however, they mainly explored low degree-of-freedom (DOF) systems, typically in the form of a linear oscillator coupled to a bistable attachment [21–24]. These studies, on both the transient dissipative dynamics under impulse excitation and the steady-state responses under harmonic excitation, unveil the potential of bistable attachments for wideband attenuation behavior. On the other hand, in metamaterial/metastructure settings, limited work has focused on nonlinear resonating configurations [25]. For example, Lazarov et al. [26] considered Duffing-type cubic hardening nonlinear resonators; Banerjee et al. [27] numerically investigated the effects of cubic hardening nonlinearity in a series of spring mass-in-mass system; Casalotti et al. [28] explored the nonlinear frequency response of a metamaterial beam with nonlinear absorbers and demonstrated enhanced vibration suppression performance. In a parallel body of work, it is also worth mentioning that interesting phenomena such as solitary wave propagation and unidirectional wave propagation have been demonstrated in bistable lattices [29–31].

Our previous work [32] considered a linear mass-spring chain with bistable attachments for a basic qualitative demonstration of amplitude-dependent bandwidth enhancement. The present work aims to move from the lumped-parameter model to a distributed-parameter model for a quantitative comparison with experiments. The paper is organized as follows. The next section presents the description of the system and the derivation of the state-space representation of the system from a distributed-parameter model based on the Euler–Bernoulli beam theory and simplified modal analysis. Numerical analysis approach combining the frequency-domain harmonic balance method and the time-domain Runge–Kutta method is briefly described in Sect. 3. Numerical studies simulating the system under low, moderate and sufficiently high intensity excitation cases are presented in Sect. 4. Select time histories of the system and the phase portraits of individual bistable attachments are plotted. Experimental results and validations are then presented for a base-excited cantilever beam hosting seven bistable magnetoelastic attachments in Sect. 5. Subsequently, a brief discussion of the work is provided along with the main conclusions of the current work.

2 Theory

The system consists of a cantilever beam under transverse vibration with S bistable attachments as shown in Fig. 1.

The beam is clamped at one end ($x = 0$) and free to vibrate at the other end ($x = L$). It has width of b, thickness of h, Young's modulus of E, and density of ρ. Each attachment is connected to the beam through a bistable spring with negative linear stiffness k_{a1} and positive cubic stiffness k_{a3}. The total transverse displacement, $w_t(x, t)$, of the cantilever beam under base excitation is defined as:

$$w_t(x, t) = w_b(t) + w(x, t) \tag{1}$$

where $w_b(t)$ is the base displacement at $x = 0$ and $w(w, t)$ is the beam displacement relative to the moving space at position x and time t. The governing equation of the beam based on Euler–Bernoulli beam theory is:

$$EI\frac{\partial^4 w(x,t)}{\partial x^4} + m\frac{\partial^2 w(x,t)}{\partial t^2} - \sum_{j=1}^{S}\left[k_{a1}w_{aj}(t) + k_{a3}w_{aj}^3(t)\right]\delta(xx_j) = -m\frac{\mathrm{d}^2 w_b(t)}{\mathrm{d}t^2} \tag{2}$$

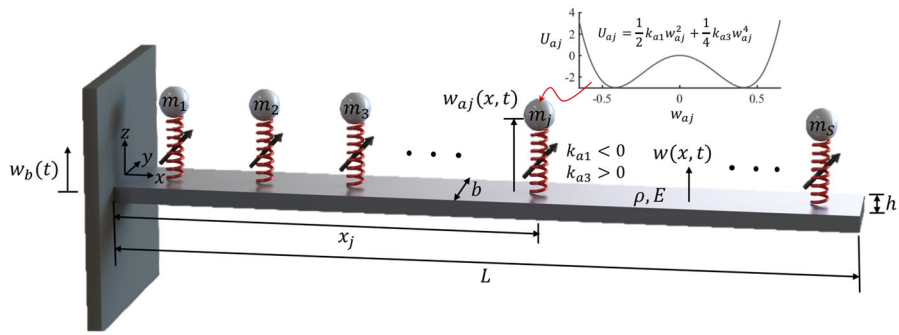

Fig. 1 Schematic of the nonlinear locally resonant metastructure (cantilever with bistable attachments) under base excitation

At this point, the system is assumed to be undamped and modal damping will be introduced at a later stage. The associated equations of motion for the attachments are:

$$m_j\left[\frac{\partial^2 w(x_j,t)}{\partial t^2} + \frac{\mathrm{d}^2 w_{aj}(t)}{\mathrm{d}t^2}\right] + k_{a1}w_{aj}(t) + k_{a3}w_{aj}^3(t) = -m_j\frac{\mathrm{d}^2 w_b(t)}{\mathrm{d}t^2}, \qquad j = 1, 2, \ldots, S \tag{3}$$

where $w_{aj}(t)$ is the relative displacement of the j-th attachment with respect to $w(x_j, t)$, x_j is the location of the j-th attachment, $I = bh^3/12$ is second moment of area about y-axis, $m = \rho bh$ is the mass per length of the beam, and m_j is the mass of the j-th attachment.

The boundary conditions of the clamped-free beam are given by:

$$w(0,t) = 0 \tag{4}$$

$$\frac{\partial w(0,t)}{\partial x} = 0 \tag{5}$$

$$EI\frac{\partial^2 w(L,t)}{\partial x^2} = 0 \tag{6}$$

$$EI\frac{\partial^3 w(L,t)}{\partial x^3} = 0 \tag{7}$$

The work mainly focuses on the frequency range in the neighborhood of one target mode (i.e., the second mode) of the cantilever beam with no attachments (plain beam). Nonlinear modal interactions are neglected since the modes of the plain beam are well separated. As mentioned in [9], an expansion using the mode shapes of a uniform clamped-free beam, $\phi(x)$, can provide a significant simplification in the analysis. The approximate solution of the displacement of the beam is:

$$w(x,t) = \sum_{r=1}^{N}\eta_r(t)\phi_r(x) \tag{8}$$

where N is the number of modes in the expansion and $\eta_r(t)$ is the modal weighting of the r-th mode of the clamped-free beam. The mass-normalized mode shapes of the beam are given by the following equation:

$$\phi_r(x) = \frac{1}{\sqrt{mL}}\left[\cos\left(\frac{\lambda_r x}{L}\right) - \cosh\left(\frac{\lambda_r x}{L}\right) + \left(\frac{\sin\lambda_r - \sinh\lambda_r}{\cos\lambda_r + \cosh\lambda_r}\right)\left(\sin\left(\frac{\lambda_r x}{L}\right) - \sinh\left(\frac{\lambda_r x}{L}\right)\right)\right], \quad r = 1, 2, \ldots, N \tag{9}$$

where λ_r is the r-th positive real solution of the characteristic equation given in Eq. (10).

$$\cos\lambda\cosh\lambda + 1 = 0 \tag{10}$$

The mode shapes of the clamped-free beam satisfy the orthogonality conditions as shown below:

$$\int_{x=0}^{x=L}\phi_r(x)m\phi_s(x)dx = \delta_{rs}, \qquad r, s = 1, 2, \ldots \tag{11}$$

$$\int_{x=0}^{x=L}\phi_r(x)EI\phi_s''''(x)dx = \omega_r^2\delta_{rs}, \qquad r, s = 1, 2, \ldots \tag{12}$$

where ω_r is the natural frequency of the r-th mode of the clamped-free beam. Substituting Eq. (8) into Eq. (2) gives the following equation:

$$EI\sum_{r=1}^{N}\eta_r(t)\phi_r''''(x) + m\sum_{r=1}^{N}\ddot{\eta}_r(t)\phi_r(x) - \sum_{j=1}^{S}\left[k_{a1}w_{aj}(t) + k_{a3}w_{aj}^3(t)\right]\delta(x - x_j) = -m\ddot{w}_b(t) \tag{13}$$

where $()'$ denotes the derivative with respect to space variable x and $\dot{()}$ denotes the derivative with respect to time t. Multiplying Eq. (13) by $\phi_s(x)$, integrating from $x = 0$ to $x = L$, and applying the orthogonality

conditions of the mode shapes shown in Eqs. (11) and (12) yield:

$$\ddot{\eta}_r(t) + \omega_r^2 \eta_r(t) - \sum_{j=1}^{S} \left[k_{a1} w_{aj}(t) + k_{a3} w_{aj}^3(t)\right] \phi_r(x_j) = -m \ddot{w}_b(t) \int_{x=0}^{x=L} \phi_r(x) \mathrm{d}x \tag{14}$$

Substitute Eq. (8) into Eq. (3) gives:

$$m_j \left[\sum_{r=1}^{N} \ddot{\eta}_r(t) \phi_r(x_j) + \ddot{w}_{aj}(t) \right] + k_{a1} w_{aj}(t) + k_{a3} w_{aj}^3(t) = -m_j \ddot{w}_b(t), \qquad j = 1, 2, \ldots, S \tag{15}$$

Given that the nonlinearity is in the relative displacement of the attachments, one we can rewrite Eq. (14) by substituting Eq. (15) as the following:

$$\ddot{\eta}_r(t) + \omega_r^2 \eta_r(t) + \sum_{j=1}^{S} m_j \phi_r(x_j) \sum_{k=1}^{N} \ddot{\eta}_k(t) \phi_k(x_j) + \sum_{j=1}^{S} m_j \ddot{w}_{aj}(t) \phi_r(x_j) = q_r(t), \qquad r = 1, 2, \ldots, N \tag{16}$$

where

$$q_r(t) = -\ddot{w}_b(t) \left(\int_{x=0}^{x=L} m \phi_r(x) \mathrm{d}x + \sum_{j=1}^{S} m_j \phi_r(x_j) \right) \tag{17}$$

To this end, Eqs. (15) and (16) form a system of $N + S$ coupled second-order ordinary differential equations. Such system can be cast into the matrix form:

$$\mathbf{M}\ddot{\mathbf{u}} + \mathbf{K}\mathbf{u} + \mathbf{G}\mathbf{u}^3 = \mathbf{F}(t) \tag{18}$$

where $\mathbf{u} = \left[\eta_1\ \eta_2 \cdots \eta_N\ w_{a1}\ w_{a2} \cdots w_{aS}\right]^\top$ contains the modal weightings of the beam and the relative displacements of the bistable attachments. The mass matrix $\mathbf{M}$, linear stiffness matrix $\mathbf{K}$ and cubic stiffness matrix $\mathbf{G}$ are:

$$\mathbf{M} = \begin{bmatrix} \mathbf{M_{11}} & \mathbf{M_{12}} \\ \mathbf{M_{21}} & \mathbf{M_{22}} \end{bmatrix}, \qquad \mathbf{K} = \begin{bmatrix} \mathbf{K_{11}} & \mathbf{0} \\ \mathbf{0} & \mathbf{K_{22}} \end{bmatrix}, \qquad \mathbf{G} = \begin{bmatrix} \mathbf{0} & \mathbf{0} \\ \mathbf{0} & \mathbf{G_{22}} \end{bmatrix}, \qquad \mathbf{F} = \begin{bmatrix} \mathbf{F_1} \\ \mathbf{F_2} \end{bmatrix}, \tag{19}$$

where $\mathbf{M_{11}}$ is a $N \times N$ matrix, with the entries: $m_{mn} = \delta_{mn} + \sum_{j=1}^{S} m_j \phi_m(x_j) \phi_n(x_j)$; $\mathbf{M_{12}}$ is a $N \times S$ matrix, with the entries: $m_{mq} = m_q \phi_m(x_q)$; $\mathbf{M_{21}}$ is a $S \times N$ matrix, with the entries: $m_{pn} = m_p \phi_n(x_p)$; $\mathbf{M_{22}}$ is a $S \times S$ matrix, with the entries: $m_{pq} = \delta_{pq} m_p$; $\mathbf{K_{11}}$ is a $N \times N$ diagonal matrix, with the entries: $k_{mn} = \delta_{mn} \omega_m^2$; $\mathbf{K_{22}}$ is a $S \times S$ diagonal matrix, with the entries: $k_{pq} = \delta_{pq} k_{a1}$; $\mathbf{G_{22}}$ is a $S \times S$ diagonal matrix, with the entries: $G_{pq} = \delta_{pq} k_{a3}$. On the right hand side of Eq. (18), the forcing vector is:

$$\mathbf{F} = \begin{bmatrix} \mathbf{F_1} \\ \mathbf{F_2} \end{bmatrix} \tag{20}$$

where $\mathbf{F_1}$ is a $N \times 1$ vector, with the entries:

$$f_m = q_m(t) = -\ddot{w}_b(t) \left[\int_{x=0}^{x=L} m \phi_m(x) \mathrm{d}x + \sum_{j=1}^{S} m_j \phi(x_j) \right] \tag{21}$$

$\mathbf{F_2}$ is a $S \times 1$ vector, with the entries: $f_p = -m_p \ddot{w}_b(t)$. For all the indices above, $m, n = 1, 2, \ldots, N$ and $p, q = 1, 2, \ldots, S$.

Equation (18) can be rearranged as:

$$\ddot{\mathbf{u}} + \mathbf{\Lambda}\mathbf{u} + \mathbf{\Psi}\mathbf{u}^3 = \boldsymbol{\delta} \tag{22}$$

where $\mathbf{\Lambda} = \mathbf{M^{-1}K}$, $\mathbf{\Psi} = \mathbf{M^{-1}G}$, $\boldsymbol{\delta} = \mathbf{M^{-1}F}$. To this end, Eq. (22) can be further turned into first-order state space form:

$$\dot{\mathbf{z}} = \mathbf{A_0 z} + \mathbf{Q z}^3 + \mathbf{R} \tag{23}$$

where

$$\mathbf{z} = \begin{bmatrix} \mathbf{u} \\ \dot{\mathbf{u}} \end{bmatrix}, \mathbf{A_0} = \begin{bmatrix} \mathbf{0} & \mathbf{I} \\ -\mathbf{\Lambda} & \mathbf{0} \end{bmatrix}, \mathbf{Q} = \begin{bmatrix} \mathbf{0} & \mathbf{0} \\ -\mathbf{\Psi} & \mathbf{0} \end{bmatrix}, \mathbf{R} = \begin{bmatrix} \mathbf{0} \\ \boldsymbol{\delta} \end{bmatrix}, \tag{24}$$

For the nonlinear spring with a negative linear stiffness ($k_{a1} < 0$) and a positive cubic stiffness ($k_{a3} > 0$), the origin ($w_{aj} = 0$) of the attachment becomes unstable and there exist two stable equilibrium points, $\bar{w}_{aj,1}$ and $\bar{w}_{aj,2}$, in the potential energy plot.

$$\bar{w}_{aj,1} = -\sqrt{-k_{a1}/k_{a3}}, \quad \bar{w}_{aj,2} = \sqrt{-k_{a1}/k_{a3}} \tag{25}$$

Table 1 System parameters

Length of the beam, L	0.889 m
Width of the beam, b	3.175 cm
Thickness of the beam, h	3.175 mm
Adjusted thickness of the beam, h_a	2.6 mm
Young's modulus of the beam, E	69 GPa
Density of the beam, ρ	2700 kg/m^3
Adjusted density of the beam, ρ_a	2970 kg/m^3
Attachment mass, m_r	36 g
Spring linear stiffness, k_{a1}	−63.451 N/m
Spring cubic stiffness, k_{a3}	634509 N/m^3
Modal damping for the beam, ζ_b	0.002
Damping ratio for the attachments, ζ_a	0.02
Number of modes in expansion, N	10
Number of attachments, S	7

Equation (15) can be linearized around either of the two stable equilibrium points, and the resulting linear natural frequency, $\bar{\omega}_a$, of the attachment is given by:

$$\bar{\omega}_a = \sqrt{-2k_{a1}/m_r} \tag{26}$$

3 Analysis approach

For the nonlinear system under harmonic base excitation, the response can exhibit periodic and aperiodic oscillations related to intrawell and interwell oscillations of the attachments. The harmonic balance method is applied to solve for the periodic steady-state solutions of η_r and w_{aj}. Since the system has cubic stiffness, the truncated Fourier series representation should contain sufficient terms and three terms are used here. Equations (27) and (28) represent the assumed three-term Fourier series expansion of the modal weighting of the r-th mode and relative displacement of j-th bistable attachment, respectively.

$$\hat{\eta}_r = a_r + \sum_{m=1}^{3} \left[A_{r,m} \cos\left(\frac{2\pi m t}{T}\right) + B_{r,m} \sin\left(\frac{2\pi m t}{T}\right) \right], \quad r = 1, 2, \ldots, N \tag{27}$$

$$\hat{w}_{aj} = a_{aj} + \sum_{m=1}^{3} \left[A_{aj,m} \cos\left(\frac{2\pi m t}{T}\right) + B_{aj,m} \sin\left(\frac{2\pi m t}{T}\right) \right], \quad j = 1, 2, \ldots, S \tag{28}$$

Since a closed-form solution is beyond reach for such a nonlinear and high DOF system, Newton–Raphson method is employed to assist finding the Fourier series expansion coefficients. More details regarding harmonic balance method can be found in [33]. Runge–Kutta method (time-domain numerical simulation) is utilized to calculate aperiodic solutions (including chaos) when Newton–Raphson method does not yield a convergent harmonic balance solution (in aperiodic response forms).

4 Numerical investigation

In the previous two sections, the system was introduced, the equations of motions were obtained and the solution strategy was described. In this section, the steady-state responses of the system are depicted as a function of frequency under various excitation amplitudes. Parameters for the case study are chosen and adjusted according to the experimental setup that will be presented in the next section. All the attachments are assumed to have the same mass, m_r, and all the springs have the same stiffness. Table 1 summarizes all the parameters of the system and the updated parameters used in the numerical investigations.

The first three resonant frequencies of the clamped-free cantilever beam without attachments (plain beam) are: 2.55 Hz, 15.9 Hz and 44.55 Hz as seen in Fig. 2. Transmissibility here and in the rest of the paper is defined as the ratio of the steady-state velocity at the tip of the aluminum beam to that at its base. Since the first three modes of the plain beam are well separated, modal interactions are neglected with a focus on the primary resonance around the mode of interest (which is the second mode).

Based on Eqs. (25) and (26), parameters of the nonlinear springs are obtained from the equilibrium positions of the bistable attachments ($\bar{w}_{aj,1} = 0.75$ cm and $\bar{w}_{aj,2} = -0.75$ cm) and the linear natural frequency around either of the equilibrium positions ($\bar{\omega}_a = 16.8$ Hz) measured in the experiments. Here, $\bar{\omega}_a$ is in the neighborhood of the second mode of the plain beam. It should be noted that the values of thickness and density for the beam used in the simulations (adjusted thickness h_a and adjusted density ρ_a) are slightly different than

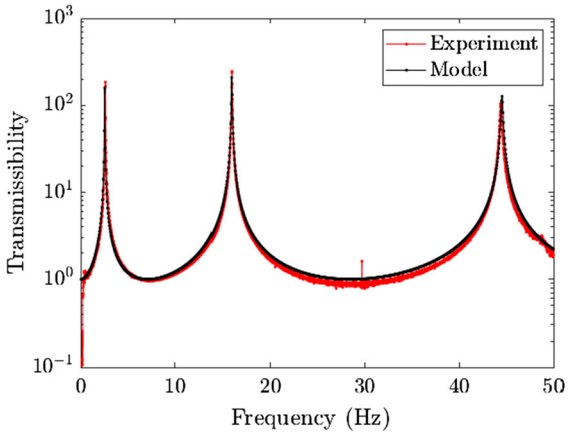

Fig. 2 Linear transmissibility of the clamped-free beam without attachments (plain beam). The first three modes are well separated. Black curve shows the simulated results based on the adjusted (updated) parameters; red curve shows the experimental data. (Color figure online)

the actual thickness and density of the beam to compensate the non-uniformity of the beam implemented in the experiments, which includes extrude cuts, holes and added point mass, etc. This is a reasonable approach given the long wavelengths in the modal neighborhood of interest. In addition, in the numerical analysis for better consistency with experiments, damping (modal damping for the beam and damping ratios for the bistable attachments) is added to the previously derived equations of motion in Eqs. (15) and (16). For simplicity, all the modes of the beam are assumed to have the same modal damping, $\zeta_r = 0.002$, and all the bistable attachments are assumed to have the same damping ratio, $\zeta_a = 0.02$. As can be seen in Fig. 2, the simulated response of plain beam based on the adjusted parameters matches very well with the measured responses in the experiments.

Since the behavior of the nonlinear system is amplitude dependent (i.e., base excitation amplitude dependent), different levels of base excitation should be explored. Four different cases are simulated and the root-mean-square (RMS) values of the base acceleration are: $0.005g$, $0.1g$, $0.3g$ and $0.5g$, where g denotes gravity. For the frequency response analysis of the nonlinear system, simulations are performed for both up and down frequency sweep at each base acceleration amplitude over the frequency range from 10 to 24 Hz. It is assumed that the beam starts from the rest and all the bistable attachments stay in the positive equilibrium positions ($\bar{w}_{aj,2} = 0.75$ cm) at the beginning of the frequency sweep as the initial conditions.

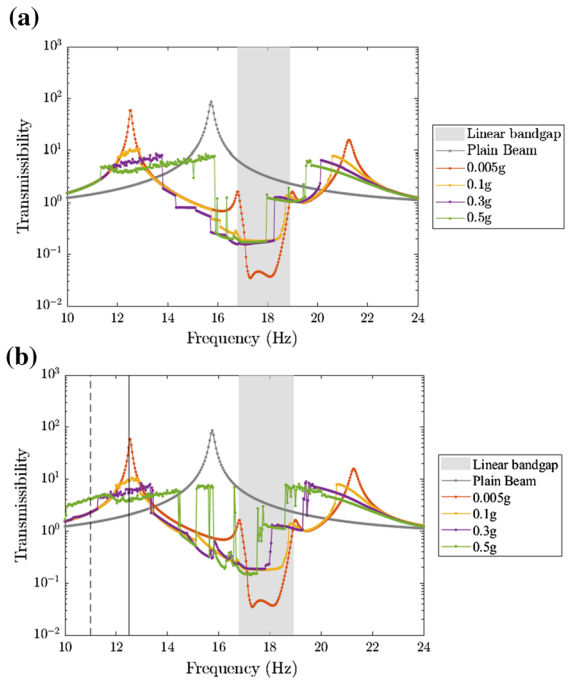

Fig. 3 Numerical simulation results for the transmissibility of the beam under different base excitation amplitudes normalized by the base acceleration: **a** up sweep and **b** down sweep

Simulated results of the transmissibility frequency response of the beam under base excitation are plotted in Fig. 3 for various RMS case acceleration levels and for both the frequency upsweep and downsweep. The shaded region in Fig. 3 shows the estimate of the linear locally resonant bandgap based on the theory developed for finite and continuous metastructures [8,9] given by:

$$\omega_t < \omega < \omega_t \sqrt{1+\mu} \tag{29}$$

where ω_t is the target frequency of the resonators and μ is the mass ratio of the total mass of the resonators to the total mass of the plain main structure as follows:

$$\mu = \frac{\sum_{j=1}^{S} m_j}{mL} = \frac{m_r S}{\rho b h L} \tag{30}$$

Here $\omega_t = \bar{\omega}_a = 16.8$ Hz and $\mu = 0.27$ are used in the plot for the system under linear behavior.

At very low base excitation amplitudes (e.g., $\ddot{w}_b = 0.005g$ RMS acceleration), the bistable attachments oscillate around the equilibrium positions at the linear natural frequency $\bar{\omega}_a$ and the system exhibits linear/quasilinear behavior, yielding a typical LR bandgap. The second mode of the plain bean is attenuated while additional resonances appear, which is similar to the behavior of just using linear locally resonant attachments. As the excitation level increases, nonlinear intrawell softening and interwell oscillations are enabled gradually. The first side peak around 12.5 Hz is reduced significantly, and a softening behavior is seen on the second side peak, achieving a broader bandwidth of attenuation. For high acceleration levels (e.g., $\ddot{w}_b = 0.5g$ RMS acceleration), wideband chaotic behavior is observed.

Select time histories of the relative displacements of all seven attachments along with the phase portraits are presented for excitation at 12.5 Hz (marked in black line in Fig. 3b) under $0.1g$, $0.3g$ and $0.5g$ RMS acceleration levels in Figs. 4, 5 and 6, respectively. For a concise demonstration, duration of 4 s time history (from 116 to 120 s) of the relative displacements of the attachments are plotted. While the phase portraits of the attachments are based on much longer time histories (from 100 to 120 s) so that the dynamics behavior of individual attachments are better captured. In addition, select time instants of the relative displacement distribution of the beam and the time average responses of the beam, $w_{\text{avg}}(x)$, from 116 to 120 s are plotted. The trend is clearly shown for gradually enabled interwell oscillations (chaotic behavior) as the excitation level increases. Under $0.1g$ RMS acceleration level (Fig. 4), attachments 1 and 5 stay within the potential well, while the other five attachments undergo interwell chaotic vibrations. The locations of the attachment indeed affect the dynamic behavior. As seen from the select time instants of the beam's response (Fig. 4c), the displacements of beam at the locations of attachments 1 and 5 are relatively small compared to the responses at the locations of the other five attachments; hence, the attachments do not escape the potential well yet for the mentioned excitation level. As the RMS acceleration level increases to $0.3g$ (Fig. 5) and $0.5g$ (Fig. 6), all the attachments begin to exhibit chaotic interwell oscillations. Higher-intensity oscillations of the bistable attachments at 12.5 Hz under $0.5g$ RMS

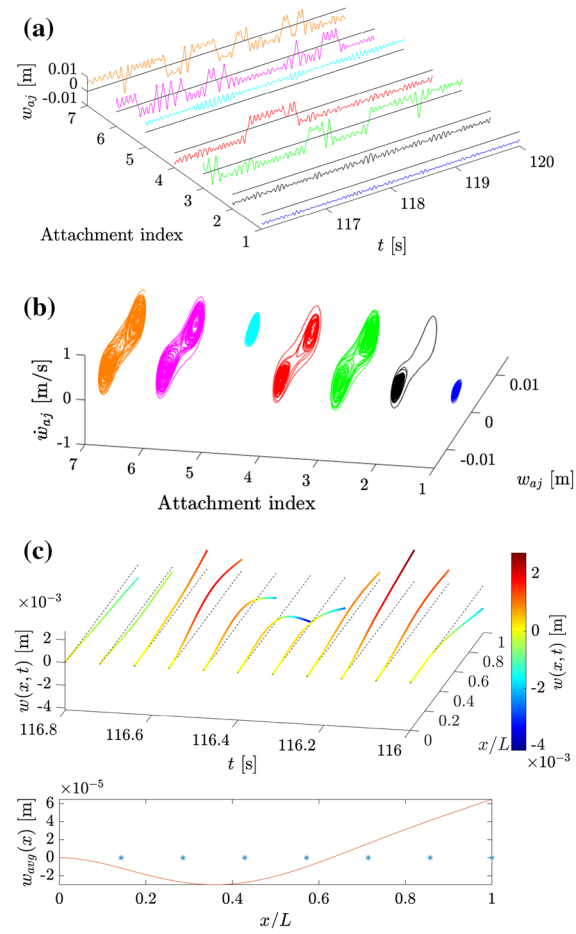

Fig. 4 Numerical simulation results for the base acceleration of $0.1g$ at 12.5 Hz. **a** Time histories and **b** phase portraits for relative displacements of the attachments. **c** Select time history of beam displacement distribution (up) and time average displacement distribution (down). Blue asterisks mark the locations of the attachments. (Color figure online)

acceleration compared to those under $0.3g$ RMS acceleration further suppress the transmissibility of the beam more as shown in Fig. 3.

Interestingly, high-energy periodic branch of the system is captured for $0.5g$ RMS acceleration level due to the large-orbit interwell oscillations of the bistable attachments. For example, as shown in Fig. 7a, b, the time histories and phase portraits of the attachments illustrate periodic interwell oscillations for $0.5g$ RMS acceleration level at 11 Hz (marked in black dash line in Fig. 3). Periodic responses of the beam itself are clearly shown in the select time instants and the time average responses of the beam displacement distribution in Fig. 7c. The responses of the beam manifest itself

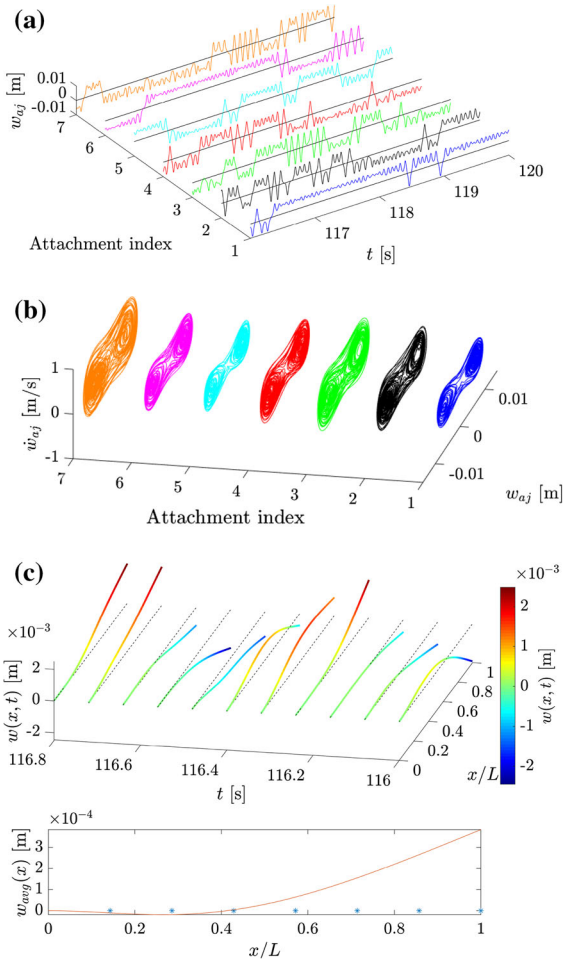

Fig. 5 Numerical simulation results for system under the base acceleration of $0.3g$ at 12.5 Hz. **a** Time histories and **b** phase portraits for the relative displacements of attachments. **c** Select time history of beam displacement distribution (up) and time average displacement distribution (down). Blue asterisks mark the locations of the attachments. (Color figure online)

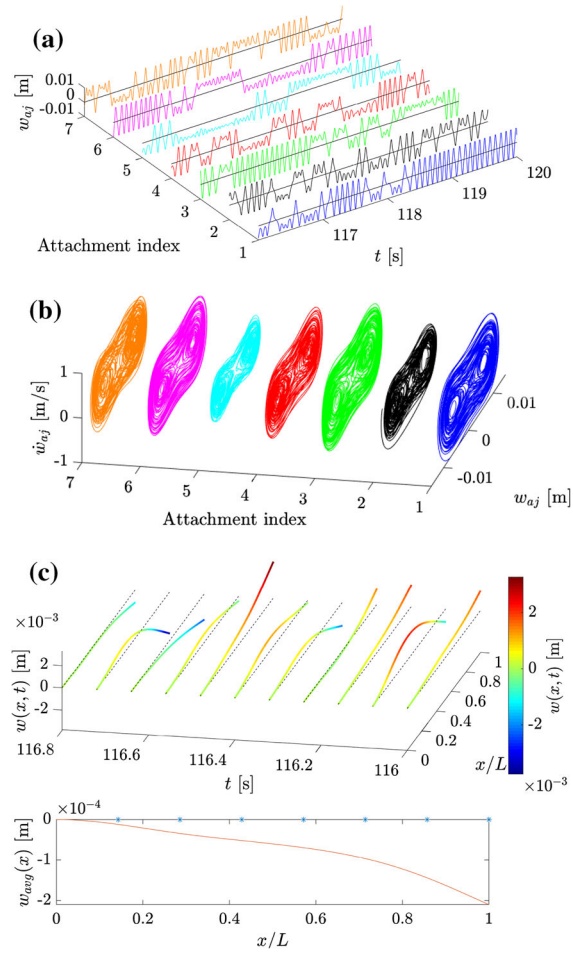

Fig. 6 Numerical simulation results for the base acceleration of $0.5g$ at 12.5 Hz. **a** Time histories and **b** phase portraits for relative displacements of the attachments. **c** Select time history of beam displacement distribution (up) and time average displacement distribution (down). Blue asterisks mark the locations of the attachments. (Color figure online)

as similar to the second mode shape of a clamped-free beam, which is the mode we are targeting.

5 Experimental validation

Experimental investigations are presented next to validate amplitude-dependent bandwidth enhancement via bistable attachments .

5.1 Experimental setup

The experimental setup shown in Fig. 8 includes an aluminum cantilever as the main structure with 7 magnetoelastic beams as bistable attachments. The main beam with the dimensions listed in Table 1 comprises 7 unit cells. Each unit cell (Fig. 8d) includes a bistable attachment made from a spring steel cantilever with tip masses. The spring steel cantilever is 9.525 mm wide, 0.254 mm thick and extending the edge of the extruded slot by 4.06 cm long. Two 9.525 mm cube-shaped permanent magnets are placed at the free end of each spring steel cantilever as tip masses. Each magnet

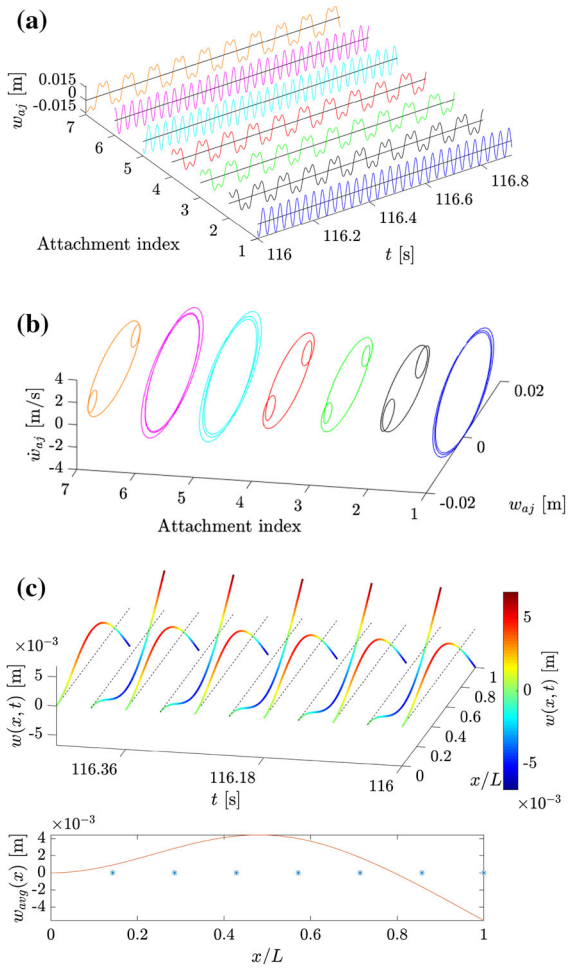

Fig. 7 Numerical simulation results for the base acceleration of $0.5g$ at 11 Hz. **a** Time histories and **b** phase portraits for relative displacements of the attachments. **c** Select time history of beam displacement distribution (up) and time average displacement distribution (down). Blue asterisks mark the locations of the attachments. (Color figure online)

has a hole through the center which is perpendicular to the magnetization direction. The other pair of two 9.525 mm cube-shaped magnets is attached on the aluminum beam to realize the bistability, and two static equilibrium positions are obtained as shown in Fig. 8e.

An APS-113 long stroke shaker driven by an APS-125 amplifier is used to excite the structure, which is clamped vertically to the armature of the shaker. For the purpose of having a constant-amplitude harmonic base acceleration at specified frequencies, a SPEKTRA VCS-201 controller is utilized, with the input from the base acceleration measured by an accelerometer. A Polytec OFV-505 laser Doppler vibrometer (LDV) oriented vertically at a 45-degree mirror measures the transverse tip velocity of the beam. The excitation frequencies are swept up from 10 to 24 Hz and down from 24 to 10 Hz at a rate of 0.25 Hz/min for four different base acceleration levels.

5.2 Experimental results

Potential wells of the bistable attachments can be adjusted by varying the locations of the magnets along the slots on the beam. The distance between the magnets is quantified by the vertical distance, d, between the lower edge of the extruded cut and the upper face of the cubic magnet as labeled in Fig. 8d. When the distance d is set to be 17 mm, the post-buckled linear natural frequency is identified to be 16.8 Hz. The equilibrium position of the attachment is measured to be 0.75 cm, which is approximated by the distance between the center of tip mass to the beam. The selection of this magnet spacing is to target the second mode neighborhood (around 15.9 Hz) of the plain beam in this work. Experiment is first performed on the plain beam, which is the main cantilever without the bistable attachments. All 7 magnetoelastic cantilevers with the corresponding pairs of magnets at the end are removed first, while all other pairs of magnets on the beam with $d = 17$ mm are still kept. The first three modes of the plain beam are plotted in the transmissibility frequency response in Fig. 2. Then, the beam with all seven bistable attachments is tested. The transmissibility frequency responses of the beam are measured for various RMS base acceleration levels, as shown in Fig. 9a, b for up and down frequency sweep, respectively.

It can be seen that the experimental results agree well with the responses predicted from the simulations (comparing Figs. 3 and 9). The shaded region shows the estimated linear locally resonant bandgap based on Eq. 29 with the target frequency $\omega_t = 16.8$ Hz and mass ratio $\mu = 0.27$. At a very low RMS base acceleration level ($0.005g$), the metastructure has a bandgap similar to the one using linear local resonators. The second mode of the plain beam is significantly attenuated, while new resonances appear. It is observed that, at such low excitation intensity level, the bistable attachments vibrate linearly (or quasilinearly) around their respective stable equilibria, staying within the potential well as expected. As the base excitation level

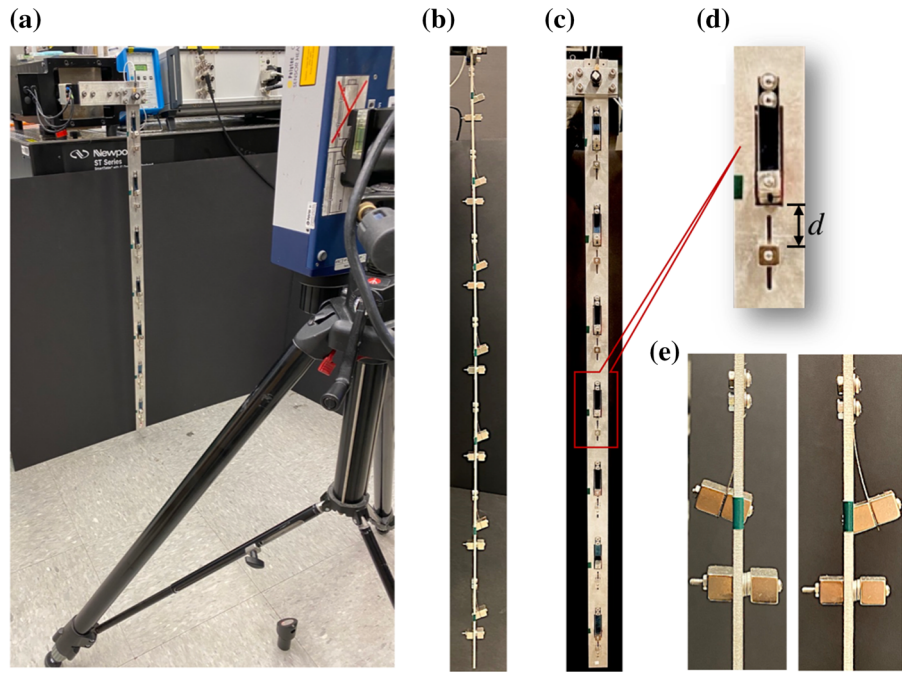

Fig. 8 **a** Overview of the experimental setup; **b** side view and **c** front view of the beam with bistable attachments; **d** close-up view and **e** static equilibrium positions of an attachment

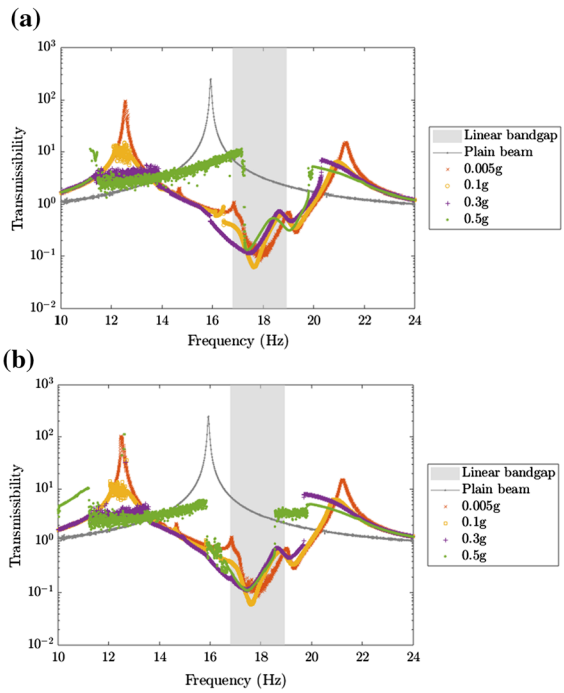

Fig. 9 Experimental results for the transmissibility of the beam under different excitation levels normalized by the base acceleration: **a** up sweep and **b** down sweep

increases, the nonlinear attenuation is triggered first by the intrawell softening of the bistable attachments. Further increase in the base excitation intensity triggers chaotic motions of the attachments, leading to bandwidth enhancement. Overall, an attenuation frequency range that is 350% wider than the corresponding linear locally resonant bandgap is observed. High energy branch at $0.5g$ RMS acceleration level is also observed in the experiments, especially in the down sweep frequency response. Slow-motion videos capturing the beam with attachments exhibiting linear intrawell, nonlinear intrawell and nonlinear interwell oscillations at select base acceleration levels and frequencies can be viewed in the Supplementary materials.

6 Discussions

In general, the experimental results agree well with the numerical results as demonstrated in the previous two sections. The small discrepancies can be caused by the following reasons. First of all, the cut-offs on the beam in the experiments are not directly considered in the simulation, which assumes the beam is uniform for simplification. Secondly, the determination of the linear and cubic terms of the stiffness is also simplified, obtained from the measurement of attachment's equilibrium positions and post-buckled linear natural frequencies. Thirdly, the existence of magnet damp-

ing from the Eddy currents can affect the responses of the beam more obviously as the base acceleration level increases when the tip magnets travel though the slots on the beam. The agreement can be further improved by modeling the system more accurately considering the aforementioned points. In addition, the clamping of the spring steel cantilever on the beam is asymmetric and the resulting double-well potential is not perfectly symmetric in the experiments (i.e., a small amount of quadratic nonlinearity is inevitable). The effect of significantly asymmetric potential wells can be found in the nonlinear energy harvesting literature [34,35]). Furthermore, small variations in manually adjusted magnet spacing are inevitable and can lead to slightly different post-buckled linear natural frequencies for the bistable attachments.

7 Conclusions

This paper investigates the rich dynamics of nonlinear locally resonant metastructures via bistable attachments both numerically and experimentally. The distributed-parameter model can be used to predict the responses of such complex system. Periodic intrawell, aperiodic intrawell, aperiodic interwell and periodic interwell oscillations of the bistable attachments are all observed under various acceleration levels. The study shows that the nonlinear interwell oscillations of the bistable attachments offer substantially wider bandwidth than the corresponding linear locally resonant bandgap. This type of nonlinear metastructures exhibits much richer dynamics and wider bandwidths than their linear counterparts whose bandgap is known to be limited by the added mass.

Acknowledgements The authors acknowledge the partial support of grant W911NF-18-1-0036 from the Army Research Office.

Compliance with ethical standards

Conflicts of interest The authors declare that they have no conflict of interest.

References

1. Liu, Z., Zhang, X., Mao, Y., Zhu, Y., Yang, Z., Chan, C.T., Sheng, P.: Locally resonant sonic materials. Science **289**(5485), 1734 (2000)
2. Li, J., Chan, C.T.: Double-negative acoustic metamaterial. Phys. Rev. E **70**(5), 055602 (2004)
3. Yu, D., Liu, Y., Wang, G., Zhao, H., Qiu, J.: Flexural vibration band gaps in Timoshenko beams with locally resonant structures. J. Appl. Phys. **100**(12), 124901 (2006)
4. Sun, H., Du, X., Pai, P.F.: Theory of metamaterial beams for broadband vibration absorption. J. Intell. Mater. Syst. Struct. **21**(11), 1085 (2010)
5. Oudich, M., Senesi, M., Assouar, M.B., Ruzenne, M., Sun, J.H., Vincent, B., Hou, Z., Wu, T.T.: Experimental evidence of locally resonant sonic band gap in two-dimensional phononic stubbed plates. Phys. Rev. B **84**(16), 165136 (2011)
6. Assouar, M.B., Senesi, M., Oudich, M., Ruzzene, M., Hou, Z.: Broadband plate-type acoustic metamaterial for low-frequency sound attenuation. Appl. Phys. Lett. **101**(17), 173505 (2012)
7. Zhu, R., Liu, X., Hu, G., Sun, C., Huang, G.: A chiral elastic metamaterial beam for broadband vibration suppression. J. Sound Vib. **333**(10), 2759 (2014)
8. Sugino, C., Leadenham, S., Ruzzene, M., Erturk, A.: On the mechanism of bandgap formation in locally resonant finite elastic metamaterials. J. Appl. Phys. **120**(13), 134501 (2016)
9. Sugino, C., Xia, Y., Leadenham, S., Ruzzene, M., Erturk, A.: A general theory for bandgap estimation in locally resonant metastructures. J. Sound Vib. **406**, 104 (2017)
10. Daqaq, M.F., Masana, R., Erturk, A., Quinn, D.D.: On the role of nonlinearities in vibratory energy harvesting: a critical review and discussion. Appl. Mech. Rev. **66**(4), 040801 (2014)
11. Erturk, A., Hoffmann, J., Inman, D.: A piezomagnetoelastic structure for broadband vibration energy harvesting. Appl. Phys. Lett. **94**(25), 254102 (2009)
12. Cottone, F., Vocca, H., Gammaitoni, L.: Nonlinear energy harvesting. Phys. Rev. Lett. **102**(8), 080601 (2009)
13. Stanton, S.C., McGehee, C.C., Mann, B.P.: Nonlinear dynamics for broadband energy harvesting: investigation of a bistable piezoelectric inertial generator. Phys. D Nonlinear Phenom. **239**(10), 640 (2010)
14. Harne, R.L., Wang, K.: A review of the recent research on vibration energy harvesting via bistable systems. Smart Mater. Struct. **22**(2), 023001 (2013)
15. Gendelman, O.V.: Bifurcations of nonlinear normal modes of linear oscillator with strongly nonlinear damped attachment. Nonlinear Dyn. **37**(2), 115 (2004)
16. Starosvetsky, Y., Gendelman, O.: Vibration absorption in systems with a nonlinear energy sink: nonlinear damping. J. Sound Vib. **324**(3–5), 916 (2009)
17. Starosvetsky, Y., Gendelman, O.: Attractors of harmonically forced linear oscillator with attached nonlinear energy sink. II: optimization of a nonlinear vibration absorber. Nonlinear Dyn. **51**(1–2), 47 (2008)
18. Parseh, M., Dardel, M., Ghasemi, M.H.: Performance comparison of nonlinear energy sink and linear tuned mass damper in steady-state dynamics of a linear beam. Nonlinear Dyn. **81**(4), 1981 (2015)
19. Kani, M., Khadem, S., Pashaei, M., Dardel, M.: Vibration control of a nonlinear beam with a nonlinear energy sink. Nonlinear Dyn. **83**(1–2), 1 (2016)
20. Silva, T.M., Clementino, M.A., De Marqui Jr, C., Erturk, A.: An experimentally validated piezoelectric nonlinear energy

sink for wideband vibration attenuation. J. Sound Vib. **437**, 68 (2018)
21. Yang, K., Harne, R., Wang, K., Huang, H.: Investigation of a bistable dual-stage vibration isolator under harmonic excitation. Smart Mater. Struct. **23**(4), 045033 (2014)
22. Manevitch, L., Sigalov, G., Romeo, F., Bergman, L., Vakakis, A.: Dynamics of a linear oscillator coupled to a bistable light attachment: analytical study. J. Appl. Mech. **81**(4), 041011 (2014)
23. Romeo, F., Sigalov, G., Bergman, L.A., Vakakis, A.F.: Dynamics of a linear oscillator coupled to a bistable light attachment: numerical study. J. Comput. Nonlinear Dyn. **10**(1), 011007 (2015)
24. Johnson, D.R., Harne, R., Wang, K.: A disturbance cancellation perspective on vibration control using a bistable snap-through attachment. J. Vib. Acoust. **136**(3), 031006 (2014)
25. Banerjee, A., Das, R., Calius, E.P.: Waves in structured mediums or metamaterials: a review. Arch. Comput. Methods Eng. **26**(4), 1029 (2019)
26. Lazarov, B.S., Jensen, J.S.: Low-frequency band gaps in chains with attached non-linear oscillators. Int. J. Non-Linear Mech. **42**(10), 1186 (2007)
27. Banerjee, A., Calius, E.P., Das, R.: The effects of cubic stiffness nonlinearity on the attenuation bandwidth of 1D elasto-dynamic metamaterials. In: ASME 2016 International Mechanical Engineering Congress and Exposition (American Society of Mechanical Engineers Digital Collection, 2016)
28. Casalotti, A., El-Borgi, S., Lacarbonara, W.: Metamaterial beam with embedded nonlinear vibration absorbers. Int. J. Non-Linear Mech. **98**, 32 (2018)
29. Nadkarni, N., Daraio, C., Kochmann, D.M.: Dynamics of periodic mechanical structures containing bistable elastic elements: from elastic to solitary wave propagation. Phys. Rev. E **90**(2), 023204 (2014)
30. Nadkarni, N., Arrieta, A.F., Chong, C., Kochmann, D.M., Daraio, C.: Unidirectional transition waves in bistable lattices. Phys. Rev. Lett. **116**(24), 244501 (2016)
31. Hwang, M., Arrieta, A.F.: Solitary waves in bistable lattices with stiffness grading: augmenting propagation control. Phys. Rev. E **98**(4), 042205 (2018)
32. Xia, Y., Ruzzene, M., Erturk, A.: Dramatic bandwidth enhancement in nonlinear metastructures via bistable attachments. Appl. Phys. Lett. **114**(9), 093501 (2019)
33. Leadenham, S., Erturk, A.: Nonlinear M-shaped broadband piezoelectric energy harvester for very low base accelerations: primary and secondary resonances. Smart Mater. Struct. **24**(5), 055021 (2015)
34. He, Q., Daqaq, M.F.: Influence of potential function asymmetries on the performance of nonlinear energy harvesters under white noise. J. Sound Vib. **333**(15), 3479 (2014)
35. Wang, W., Cao, J., Bowen, C.R., Inman, D.J., Lin, J.: Performance enhancement of nonlinear asymmetric bistable energy harvesting from harmonic, random and human motion excitations. Appl. Phys. Lett. **112**(21), 213903 (2018)